Semi-Supervised Learning of Lift Optimization of Multi-Element Three-Segment Variable Camber Airfoil

Upender K. Kaul* and Nhan T. Nguyen**
NASA Ames Research Center, USA.

This chapter describes a new intelligent platform for learning optimal designs of morphing wings based on Variable Camber Continuous Trailing Edge Flaps (VCCTEF) in conjunction with a leading edge flap called the Variable Camber Krueger (VCK). The new platform consists of a Computational Fluid Dynamics (CFD) methodology coupled with a semi-supervised learning methodology. The CFD component of the intelligent platform comprises of a full Navier-Stokes solution capability (NASA OVERFLOW solver with Spalart-Allmaras turbulence model[1]) that computes flow over a tri-element inboard NASA Generic Transport Model (GTM) wing section. Various VCCTEF/VCK settings and configurations were considered to explore optimal design for high-lift flight during take-off and landing. To determine globally optimal design of such a system, an extremely large set of CFD simulations is needed. This is not feasible to achieve in practice. To alleviate this problem, a recourse was taken to a semi-supervised learning (SSL) methodology,[2] which is based on manifold regularization techniques.[3] A reasonable space of CFD solutions was populated[4] and then the SSL methodology was used to fit this manifold in its entirety, including the gaps in the manifold where there were no CFD solutions available.

The SSL methodology in conjunction with an elastodynamic solver (FiDDLE[5]) was demonstrated in an earlier study involving structural health monitoring.[6] These CFD-SSL methodologies define the new intelligent platform that forms the basis for our search for optimal design of wings. Although the present platform can be used in various other design and operational problems in engineering, this chapter focuses on the high-lift study of the VCK-VCCTEF system.

Top few candidate design configurations were identified by solving the CFD problem in a small subset of the design space. The SSL component was trained on the design space, and was then used in a predictive mode to populate a selected set of test points outside of the given design space. The new design test space thus populated was evaluated by using the CFD component by determining the error between the SSL predictions and the true (CFD) solutions, which was found to be small. This demonstrates the proposed CFD-SSL methodologies for isolating the best design of the VCK-VCCTEF system, and it holds promise for quantitatively identifying best designs of flight systems, in general.

1 Introduction

The Advanced Air Transportation Technologies (AATT) project is conducting multidisciplinary foundational research to investigate advanced concepts and technologies for future aircraft systems under the Advanced Air Vehicle Program (AAVP) of the NASA Aeronautics Research Mission Directorate. A NASA study entitled "Elastically Shaped Future Air Vehicle Concept" was conducted in 2010[7,8] to examine new concepts that can enable active control of wing aeroelasticity to achieve drag reduction. This study showed that highly flexible wing aerodynamic surfaces can be elastically shaped in-flight by active control of wing twist and vertical deflection in order to optimize the local angle of attack of wing sections. Thus aerodynamic efficiency can be improved through drag reduction during cruise and enhanced lift performance during take-off and landing.

* Computational Aerosciences Branch, NASA Advanced Supercomputing (NAS) Division; Associate Fellow, AIAA

** Intelligent Systems Division; Associate Fellow, AIAA

The study shows that active aeroelastic wing shaping control can have a potential drag reduction benefit. Conventional flap and slat devices inherently generate drag as they increase lift. The study shows that in cruise, conventional flap and slat systems are not aerodynamically efficient for use in active aeroelastic wing shaping control for drag reduction. A new flap concept, referred to as Variable Camber Continuous Trailing Edge Flap (VCCTEF) system, was conceived by NASA to address this need.[7] Initial study results indicate that the VCCTEF system may offer a potential pay-off in drag reduction in cruise that could provide significant fuel savings. Fig. 1 illustrates the VCCTEF deployed on the NASA generic transport model (GTM).

NASA and Boeing are currently conducting further studies of the VCCTEF under the research element Performance Adaptive Aeroelastic Wing (PAAW) within the AATT project.[9,10] This study built upon the development of the VCCTEF system (shown in Fig. 2) for the GTM[11] employs light-weight shaped memory alloy (SMA) technology for actuation and three separate chordwise flap segments shaped to provide a variable camber to the flap. Introduction of this camber has potential for drag reduction as compared to a conventional straight, plain flap. The flap is also made up of individual 2-foot spanwise sections, which enable different flap settings at each flap spanwise position. This enables wing twist shape control as a function of span to establish the best lift-to-drag ratio (L/D) at any aircraft gross weight or mission segment. Current wing twist on commercial transports is permanently set for one cruise, which is usually a 50% fuel loading or mid-point on the gross weight schedule. The VCCTEF offers different wing twist settings for each gross weight condition and also different settings for climb, cruise and descent, which is a major factor in obtaining the best L/D for all gross weight conditions and phases of flight. The second feature of VCCTEF is a continuous trailing edge. The individual 2-foot spanwise flap sections are connected with a flexible covering, so no breaks can occur in the flap platform, thus reducing excessive vorticity generation. This can reduce drag and airframe noise. Variable camber when combined with the continuous trailing edge results in a further reduction in drag.

The continuous trailing edge flap design combined with variable camber flap can result in lower drag. In summary, it can also offer a potential noise reduction benefit due to distinct optimal settings for climb, cruise and descent.[12] In a previous paper,[13] a computational study was conducted to explore the two-dimensional viscous effects in cruise of a number of VCCTEF configurations on lift and drag of the GTM wing section at the wing planform break. The NASA flow solver OVERFLOW was used to conduct this study. The results identified the most aerodynamically efficient VCCTEF configuration among the initial candidates. The study also showed that a three-segment variable camber flap is aerodynamically more efficient than a single-element plain flap. A recent high-lift wind tunnel test conducted in July 2014 at University of Washington Aeronautical Laboratory[14,15] confirms this observation.

The present study builds on a recent RANS study[4] that explored the high-lift design space for the tri-element airfoil typical of a GTM wing section. The tri-element airfoil is comprised of VCK, main airfoil and the VCCTEF. The design space consists of 224 configurations drawn from various combinations of of VCK and VCCTEF settings, as described below. Limited experimental data[15,16,17] are available corresponding to four configurations (VCK65, VCK60, VCK55, VCK50 – $vck1$), out of the 224 considered here using CFD. In the following paragraphs, details of the CFD results will be presented, followed by the details of the semi-supervised learning methodology and results.

The database of solutions generated by CFD simulations is a subset of a very large manifold of possible solutions, which would be impractical to generate using CFD. Therefore, a semi-supervised machine learning methodology,[2,3] which is based on three regularization terms, i.e., least squares, a Laplacian and a radial basis function will be used to approximate this manifold of solutions, as shown below. This methodology was demonstrated in the context of structural fault detection.[6] This semi-supervised learning methodology relies on its Laplacian component to smoothly approximate the manifold over gaps in the solution manifold created by a finite number of CFD solutions sparsely populating the solution manifold and is guaranteed to converge with the appropriate choice of kernel parameters.[3] The regularization concept, in general, owes its origin to Ref. 18, and it is widely used in learning techniques, unsupervised and fully supervised. This chapter focuses on the use of the semi-supervised learning algorithm[3], called the Laplacian Regularized Least Squares algorithm.

2 Methodology

The methodology proposed in the present work is multi-disciplinary in nature. The first component is based on modeling and simulation of candidate configurations of the VCK-VCCTEF system under consideration using CFD. The second component is based on learning the sparse database created in the first component and then providing as large a database as desired through a semi-supervised learning process, within a small error bound. The third component is the wind-tunnel validation of this large database at various desired test points. The third component is not the subject of the present work. The first two components will provide a host of design test points for the experimentalist to validate. The approach adopted here establishes a viable design methodology that will converge onto optimal designs of the VCK-VCCTEF system in much shorter time than would be possible otherwise. In fact, converging onto an optimal design would not be practically feasible, without the semi-supervised learning component. We shall call the first component RANS simulations and the second component Semi-supervised Learning, and they are described below.

2.1 RANS Simulations

The high-lift flow field was simulated for M = 0.25 and Re = 3.3196x10^7, where M represents the Mach number and Re the Reynolds number, based on the chord length. RANS simulations, based on the OVERFLOW flow solver with the SA turbulence model, were carried out to generate steady state solutions. Numerous combinations corresponding to 18 vck configurations for VCK setting (deflection angle) of 55^o and 19 vck configurations each for VCK settings of 60^o and 65^o with respect to the main wing, and 4 VCCTEF settings with the Fowler slot for the inboard wing are considered in this study. These vck configurations along with the 4 VCCTEF settings are represented in Table 1 below. Three VCK settings are considered, corresponding to deflection angles of 55^o, 60^o and 65^o. For each VCK setting, VCK55, VCK60 and VCK65, the vck configurations in terms of x and y displacement offset with respect to one experimental configuration (VCK65 + vck1) studied experimentally are shown in Fig. 3, Fig. 4 and Fig. 5, respectively. Nineteen vck configurations are designated vck1, vck2, vck3, ... , vck18, vck19. Detailed computational results discussing the lift characteristics will be shown below for all the 224 configurations to explore better design than the four studied experimentally.

Fig. 6 shows the four VCCTEF settings, corresponding to 4 different flap deflection angles, as shown in Table 2. Definition of various configurations are listed in Table 1. The four VCCTEF settings are denoted by 10/10/10, 15/10/5, 20/5/5 and 30/0/0. These settings were selected based on a total deflection angle of 30^o, a value which is typically used in landing and take-off configurations. The VCCTEF settings include a circular arc, a parabolic arc and a straight deflected flap.

2.2 Semi-supervised Learning

The purpose of the learning methodology is to fill the gap in the space of a relatively small set of solutions that can be reasonably obtained by CFD owing to large computational resources needed. Using the solution space corresponding to 224 configurations populated by CFD, we fit a multi-dimensional "surface" over this space and thus enable solutions at all intermediate configurations.

We do a random selection of a subset of these CFD solutions and strip off the C_{lmax} values, where C_l represents the lift coefficient, from this subset and call this subset unlabelled (u) data, in the parlance of semi-supervised learning.[3] We will refer to the rest as labelled (l) data. Similarly, we select the unlabelled (u) and labelled data (l) for C_{dmax}, where C_d represents the drag coefficient. Following,[15] we write an expression for our objective function:

$$f^* = \min_{f \in H_K} \frac{1}{l} \Sigma_{i=1}^{l} (y_i - f(x_i))^2 + \gamma_A ||f||^2{}_K + \frac{\gamma_I}{(u+l)^2} \mathbf{f}^T L \mathbf{f} \text{.....(1)}$$

where for a Mercer Kernel, K: X x $X \rightarrow R$, $\exists$ a reproducing kernel Hilbert space (RKHS), H_K of functions $X \rightarrow R$, with a norm $\| \quad \|_K$, and where the first term, $(y_i - f(x_i))^2$ is a squared loss function representing a least squares regularizer, the second term represents a radial basis function based regularizer and the third term is a Laplacian based regularizer. The optimization problems are solved for different

training sets that define the cost function (squared loss function shown in Eq. 1 above) and different choices of the regularization parameters, γ_A and γ_I.

The Representer Theorem can be used to show that the minimization problem has solution in H_K, and it is given by an expansion of kernel functions over both the labeled (l) and the unlabeled (u) data:

$$f^*(x) = \Sigma_{i=1}^{l+u} \alpha^*{}_i K(x, x_i) \text{.....(2)}$$

Minimization process of the objective function shown above constitutes a Laplacian regularized least squares algorithm.[3] The labeled data are $\{(x_i, y_i)\}_{i=1}^{l}$, and the unlabeled data are $\{(x_j)\}_{j=l+1}^{j=l+u}$. By minimizing the objective function given by Eq. (1) above, we arrive at our solution over all the points in the domain of our interest with known error bounds, which is an advantage over other methods such as artificial neural networks (ANN). In addition, the convergence to this global minimum over the considered training set is guaranteed.[15] A convex differentiable objective function of the $(l + u)$ dimensional variable, $\alpha = [\alpha_1, ...\alpha_{l+u}]^T$, is obtained by substituting Eq. (2) in Eq. (1) above, which gives us

$$\alpha^* = (JK + \gamma_A lI + \frac{\gamma_I l}{(u+l)^2} LK)^{-1} Y \text{.....(3)}$$

where J is a diagonal matrix and K is the Gram matrix of size, $(l+u)$ x $(l+u)$. In J; the first l diagonal entries are 1 and the remaining are 0. Y is a vector of size, $(l+u)$ and L is the graph Laplacian. For further details, the reader is referred to Ref. 3.

Thus, the solution to the optimization problem is obtained via Eq. 2 and Eq. 3 above.

Table 1: Definition of *vck*-VCCTEF Configurations

vck Configuration	10/10/10	15/10/5	20/5/5	30/0/0
*vck*1	*vck*1+10/10/10	*vck*1+15/10/5	*vck*1+20/5/5	*vck*1+30/0/0
*vck*2	*vck*2+10/10/10	*vck*2+15/10/5	*vck*2+20/5/5	*vck*2+30/0/0
*vck*3	*vck*3+10/10/10	*vck*3+15/10/5	*vck*3+20/5/5	*vck*3+30/0/0
*vck*4	*vck*4+10/10/10	*vck*4+15/10/5	*vck*4+20/5/5	*vck*4+30/0/0
*vck*5	*vck*5+10/10/10	*vck*5+15/10/5	*vck*5+20/5/5	*vck*5+30/0/0
—	————	————	————	————-
—	————	————	————	————-
—	————	————	————	————-
*vck*19	*vck*19+10/10/10	*vck*19+15/10/5	*vck*19+20/5/5	*vck*19+30/0/0
		vck configurations are represented in Fig. 4, Fig. 5 and Fig. 6		

Table 2: Definition of VCCTEF Configurations

Configuration	Notation	Flap 1, deg	Flap 2, deg	Flap 3, deg
3-segment circular arc camber	10/10/10	10	10	10
3-segment semi-rigid arc camber	15/10/5	15	10	5
3-segment	20/5/5	20	5	5
1-segment rigid flap	30/0/0	30	—	—
	Flap deflection angles are relative to the upstream segments			

3 Results

Results corresponding to CFD simulations will be discussed first, followed by the results obtained by the learning methodology.

3.1 CFD Results

The results of the CFD study of lift optimization were discussed in an earlier study[4], where a detailed grid sensitivity study was carried out. An optimal grid resolution was determined to be 436x106x3 for the VCK, 694x106x3 for the main wing and 471x106x3 for the VCCTEF. For further details, the reader is referred to Ref. 4.

A total of 4x(19x2+18x1) = 224 cases (19 *vck* configurations for each of the two VCK settings, VCK65 and VCK60, 18 *vck* configurations for the VCK55 setting, all corresponding to 4 different VCCTEF settings) are considered. A sweep of angle of attack ranging from from -5 deg to 20 deg is considered. There are only 18 *vck* configurations in the case of VCK55, since the 19th configuration is unrealistic for this case, as mentioned above.

Instead of showing the results for all the 224 cases individually, 3D bar graphs are shown in Fig. 7 and Fig. 8 for the case of the VCCTEF 10/10/10 setting corresponding to C_{lmax} and C_{dmax}, respectively. These 3D bar graphs give a consolidated view of C_{lmax} and C_{dmax} for all the 56 configurations corresponding to the 10/10/10 setting of VCCTEF. Similarly, 3D bar graphs for the case of VCCTEF 15/10/5 are shown in Fig. 9 and Fig. 10, for the case of VCCTEF 20/5/5 in Fig. 11 and Fig. 12, and for the 30/0/0 case in Fig. 13 and Fig. 14, respectively. The 3D bar graphs lay out a picture that presents the CFD data that defines a subset of the manifold of solutions which the learning methodology will approximate.

For a closer picture of the variation of C_{lmax} and C_{dmax}, it will be necessary to show 2D bar graphs. We will therefore show the 2D bar graphs for all the VCCTEF settings, in discussion of our results. A 2D bar graph is first presented showing C_{lmax} for the VCCTEF-10x10x10 setting in Fig. 15. Corresponding plot for C_{dmax} is shown in Fig. 16. Fig. 15 gives an overall view of the lift performance of the VCCTEF-10x10x10 setting for all the *vck* configurations corresponding to VCK55 and VCK60 and VCK65, and Fig. 16 shows corresponding results for C_{dmax}. Similarly, Fig. 17 and Fig. 18 show C_{lmax} and C_{dmax}, respectively, for the VCCTEF-15x10x5 setting. Fig. 19 and Fig. 20 show the corresponding results for the VCCTEF-20x5x5 setting, and Fig. 21 and Fig. 22 show the corresponding results for the VCCTEF-30x0x0 setting. Figs. 15 through 22 give an overall view of the C_{lmax} and C_{dmax} results for all the cases considered. The details of why these *vck* configurations yield distinctly different lift characteristics will be presented in a separate study, where the corresponding flow fields will be studied in detail. The present work is focussed on the design aspects of the problem.

Results for C_l vs α are shown for a subset of these 224 cases. For this purpose, cases giving the 4 largest values of C_{lmax} are selected from Fig. 15 through Fig. 22. It turns out that for the VCK55 setting, *vck* configurations of 2, 4, 14 and 15 give the largest C_{lmax} for all the four VCCTEF settings of 10x10x10, 15x10x5, 20x5x5 and 30x0x0, and for VCK60 and VCK65 settings, *vck* configurations of 2, 7, 15 and 19 give the largest C_{lmax} for all the four VCCTEF settings. Therefore, in the discussion of results below, only these *vck* configurations will be considered.

The determination of C_{lmax} and C_{dmax} is made by inspecting the lift curve and drag polar results. For example, for the VCK65 setting, C_{lmax} and C_{dmax} as shown in Fig. 23(a) and Fig. 23(b), respectively. Representative C_{lmax} and C_{dmax} are shown in Fig. 24, Fig. 25 and Fig. 26, for the VCK55, VCK60 and VCK65 settings, respectively, and the case of VCCTEF-20x5x5 setting. From Fig. 23(a) and Fig. 23(b), it is shown that a constant lift curve slope exists only beyond $\alpha = 0$, which shows that at lower angles of attack, the lift curve for the tri-element VCK-wing-VCCTEF system does not follow linear theory. This is shown by a nonlinear lift curve in the α range below 0 deg.

Fig. 24(a,b) shows the C_l vs α and drag polar results, respectively, for the VCK55 and VCCTEF-20x5x5 settings corresponding to *vck*2, *vck*4, *vck*14 and *vck*15 configurations. The *vck*15 case outperforms the other three, based on maximum C_l. As mentioned above, in high-lift flight configuration, we want to minimize the stall speed, which can be accomplished by maximizing C_l. The *vck*15 case also performs the best for the other three VCCTEF settings, 15x10x5, 20x5x5 and 30x0x0 for the VCK55 setting, not shown here. .

The situation is different for the VCK60 setting, where the best lift performance (C_{lmax} is demonstrated by the *vck*2 case for all the VCCTEF settings. For example, for the VCCTEF-20x5x5 setting, highest C_{lmax} corresponds to the *vck*2 configuration, as shown in Fig. 25. This also holds true for the other three VCCTEF settings. For the VCK65 setting, best lift performance is demonstrated again by the *vck*15 configuration for all the VCCTEF settings. For example, this result is shown for the VCCTEF-20x5x5 setting in Fig. 26. The overall result for the VCK60 setting is shown in Fig. 25(a), where *vck*2 and *vck*15 configurations yield

the best and the next best high lift performance. For the VCK65 setting, the overall result is shown in Fig. 26(a), where $vck15$ and $vck2$ configurations yield the best and the next best high lift performance.

It is shown that $vck15$ and $vck2$ configurations are the top two candidates, in terms of overall high lift performance, out of all the three VCK settings (VCK55, VCK60 and VCK65) for the VCCTEF-20x5x5 setting. Fig. 27(a) further shows that the VCCTEF-30x0x0 setting gives the highest lift performance ($C_l - \alpha$) corresponding to $vck15$ and $vck2$ configurations out of all the 4 VCCTEF settings.

3.2 Semi-supervised Learning Results

The CFD solutions for C_{lmax} and C_{dmax} for the 224 VCK-VCCTEF configurations are shown in Fig. 7 through Fig. 27. The semi-supervised learning is based on these 224 configurations. We now pick a small subset of test configurations outside of these 224 configurations for testing the learning methodology. These test configurations are shown in Fig. 28(a,b,c) for the case of VCK55, VCK60 and VCK65 settings, respectively. The learning algorithm will be tested on these nine configurations for the three VCK settings corresponding to the VCCTEF-30/0/0 setting. The test metrics quantifying the accuracy of the learning methodology are chosen to be root-mean-square (rms) error, rms error normalized by standard deviation and rms error normalized by maximum deviation. This will be discussed below.

First, we will report the results corresponding to fully supervised learning, i.e., the complete manifold has no unlabelled points. Fig. 29(a,b,c) shows the results for C_{lmax} corresponding to VCK55, VCK60 and VCK65 settings, respectively. The predictions approximate the CFD solutions (true solutions) within the rms error bound of about 5%. This is a good approximation, given that the training space is populated with just 224 solutions. For our purpose here, it is sufficient to use this limited training set, since our predictions will be used to define a new design space to be eventually validated by wind-tunnel experiments. In Fig. 29(a), for the case of VCK55, the largest discrepancy is approximately 7%, which is still close to the statistical error margin of 5%. Knowing the nature of the data from CFD computations, a test set could be chosen selectively to reduce this error further. But, in general, especially for a large database, a deterministic selection of a test set may not be feasible. So, a test set is chosen here deliberately to stress-test the learning algorithm.

Fig. 30(a,b,c) shows the corresponding C_{lmax} results for semi-supervised learning, with unlabelled space being a small subset (10%, chosen randomly) of the 224 solutions. On comparison of Figs. 29 and 30, it is shown that for VCK55 and VCK60 settings, the semi-supervised learning appears to give better predictions than the fully supervised learning. In fact, this difference in predictions corresponding to the fully supervised and semi-supervised learning falls within the statistical error margin and is influenced by the choice of random selection of the unlabeled data. For VCK65 setting, the comparison between fully supervised and semi-supervised learning shows a similar prediction accuracy. Overall, the semi-supervised learning yields predictions as well as the fully supervised learning, allowing for the statistical error margin of 5%, as stated above. This is in keeping with the expectation that the Laplacian component of the learning algorithm approximate the manifold over the unlabelled points as well as the fully supervised algorithm.

Similar behavior of the learning model is shown for C_{dmax} through Fig. 31(a,b,c) and Fig. 32(a,b,c). Fig. 31(a,b,c) shows results corresponding to the fully supervised learning, and Fig. 32(a,b,c) corresponding to the semi-supervised learning. Again, the rms error between the predictions and the true solution is within 5%.

Semi-supervised learning was also used with the unlabelled space as 20% of the 224 solutions. The predictions were slightly degraded as compared with the 10% unlabelled space. This comparison for C_{lmax} is shown in Table 3, where three different measures of error are compared corresponding to fully supervised and semi-supervised learning: root mean square (rms), rms error normalized by the standard deviation and rms error normalized by the difference in maximum and minimum of C_{lmax}. Differences in results with fully supervised and semi-supervised learning are within a 5% spread. Even though the VCK55 and VCK60 predictions appear to be slightly better for the semi-supervised case, this difference is not statistically significant. It should be mentioned here that the unlabeled data set is chosen randomly. Corresponding results for C_{dmax} are shown in Table 4. Again, the errors are statistically similar.

Finally, Table 5 shows a comparison of the execution time among the CFD, fully supervised and semi-supervised solution methodologies. Whereas, each CFD solution takes about 310 sec on a 480 processor Pleiades supercomputer in the NAS facility, fully supervised and semi-supervised learning methodologies

take less than 1 sec on a MacBook Pro laptop.

Table 3: Different Error Measures for C_l

Algorithm	rms	rms/std	rms/(max(Cl_{max}) − $min(Cl_{max})$)
Fully Supervised	0.0461	1.2241	0.4332
Semi-supervised (U=10%)	0.0477	1.2665	0.4482
Semi-supervised (U=20%)	0.0637	1.6918	0.5988

Table 4: Different Error Measures for C_d

Algorithm	rms	rms/std	rms/(max(Cl_{max}) − $min(Cl_{max})$)
Fully Supervised	0.0314	0.1263	0.0468
Semi-supervised (U=10%)	0.0282	0.1137	0.0421
Semi-supervised (U=20%)	0.0358	0.1443	0.0534

Table 5: Comparison of Execution Time

CFD	Fully Supervised Learning	Semi-supervised Learning
310 sec	0.8 sec	0.9 sec

4 Summary

In this chapter, a detailed CFD high-lift study of the VCK-VCCTEF system has been carried out to study the viscous effects in take-off and landing to explore the best VCK-VCCTEF system designs. For this purpose, a three-segment variable camber airfoil employed as a performance adaptive aeroelastic wing shaping control effector for a NASA Generic Transport Model (GTM) in landing and take-off configurations was considered. The objective of the study was to define optimal high-lift VCCTEF settings and VCK settings/configurations. A total of 224 combinations of VCK settings/configurations and VCCTEF settings were considered for the inboard GTM wing, where the VCCTEFs are configured as a Fowler flap that forms a slot between the VCCTEF and the inboard section of the main wing. For the VCK settings of deflection angles of 55^o, 60^o and 65^o, 18, 19 and 19 vck configurations, respectively, were considered for each of the 4 different VCCTEF deflection settings. Different VCK configurations were defined by varying the horizontal and vertical distance of the vck from the main wing. We have identified two topmost *vck* configurations corresponding to each of the three VCK settings, out of the 224 configurations considered. For all the VCK settings, *vck*2 and *vck*15 give the best lift performance, regardless of the four VCCTEF settings used. In particular, the VCCTEF-30x0x0 setting gave the highest overall lift performance with the *vck*2 and *vck*15 configurations. Thus, the best configurations for the GTM airfoil have been identified out of all the 224 cases studied. This provides a useful guide for the wind-tunnel experiment to verify the best design GTM configurations. Some of these best high-lift configurations offer a counter-intuitive design that would not have been considered experimentally *a priori*.

Since only a small subset of a very large set of possible configurations was considered using CFD, due to a prohibitive computational expense and time limitations, the semi-supervised learning (SSL) methodology was adopted as a supplementary tool to circumvent these problems. Using the SSL methodology, high lift study of 9 additional configurations of the VCK-VCCTEF system was carried out. The predicted C_{lmax} and C_{dmax} results obtained with the SSL methodology were shown to be close to the true (CFD) solutions, within the rms error bound of 5%. This demonstrates the feasibilty of the semi-supervised learning as a design tool for identifying the best performing candidate VCK-VCCTEF configurations very rapidly, in conjunction with CFD simulations and wind-tunnel experiments. It should be noted here that the size of the unlabelled

data was picked to be 10% by also selecting another number, 20%, which underperformed the number, 10%. This number tends to have an inverse relation to the degree of sparsity of CFD database.

Thus, the SSL methodology for the design problem at hand is well established to rapidly populate an arbitrarily large design space and predict C_{lmax} and C_{dmax} corresponding to the new test points. This reinforces the overall CFD-SSL design methodology adopted here and provides a viable tool for design problems in the wing design. It is encouraging to note that the SSL methodology used here is independent of a particular design system. In fact, it can be extended to solve a variety of design problems in engineering.

5 Acknowledgement

The authors would like to thank the Advanced Air Transport Technology Project under the Advanced Air Vehicles Program of the NASA Aeronautics Research Mission Directorate (ARMD) for funding support of this work. The authors also would like to acknowledge Boeing Research and Technology and the University of Washington for their collaboration with NASA under NASA contract NNL11AA05B task order NNL12AD09T entitled "Development of Variable Camber Continuous Trailing Edge Flap System for B757 Configured with a More Flexible Wing."

6 References

[1]Spalart, P. R., and Allmaras, S. R., "A One-Equation Turbulence Model for Aerodynamic Flows," AIAA 92-0439, AIAA 30th Aerospace Sciences Meeting and Exhibit, Reno, NV , January 1992.

[2]Kaul, U. K., "A Kernel-based Semi-supervised Machine Learning Methodology," Internal NASA Report, NASA Ames Research Center, June 20, 2005

[3]Belkin, M., Niyogi, P. and Sindhwani, V., "Manifold Regularization: A Geometric Framework for Learning from Examples," Journal of Machine Learning Research 7 (2006) 2399-2434; also Internal Report, The University of Chicago, Chicago, August 2004

[4]Kaul, U. K. and Nguyen, N. T., "Lift Optimization Study of a Multi-Element Three-Segment Variable Camber Airfoil," AIAA 2016-3569, 34th Applied Aerodynamics Conference, AVIATION 2016 Forum, June 13 - 17, 2016, Washington, D.C.

[5]Kaul, U. K., "FiDDLE: A Computer Code for Finite Difference Development of Linear Elasticity in Generalized Curvilinear CoordinatesÓ, NASA/TM-2005 - 213450, January 2005

[6]Kaul, U. K. and Oza, N. C., "Machine Learning for Detecting and Locating Damage in a Rotating Gear," SAE Transactions, Paper 2005-01-3371, 2005; also SAE J. Aerospace, 2005

[7]Nguyen, N., "Elastically Shaped Future Air Vehicle Concept," NASA Innovation Fund Award 2010 Report, October 2010, Submitted to NASA Innovative Partnerships Program. http://ntrs.nasa.gov/archive/nasa/casi.ntrs.nasa.g

[8]Nguyen, N., Trinh, K., Reynolds, K., Kless, J., Aftosmis, M., Urnes, J., and Ippolito, C., "Elastically Shaped Wing Optimization and Aircraft Concept for Improved Cruise Efficiency," AIAA Aerospace Sciences Meeting, AIAA-2013-0141, January 2013.

[9]Boeing Report No. 2012X0015, "Development of Variable Camber Continuous Trailing Edge Flap System," October 4, 2012.

[10]Urnes, J., Nguyen, N., Ippolito, C., Totah, J., Trinh, K., and Ting, E., "A Mission Adaptive Variable Camber Flap Control System to Optimize High Lift and Cruise Lift to Drag Ratios of Future N+3 Transport Aircraft," AIAA Aerospace Sciences Meeting, AIAA-2013-0214, January 2013.

[11]Jordan, T. L., Langford, W. M., Belcastro, C. M., Foster, J. M., Shah, G. H., Howland, G., and Kidd, R., "Development of a Dynamically Scaled Generic Transport Model Testbed for Flight Research Experiments," AUVSI Unmanned Unlimited, Arlington, VA, 2004.

[12]Nguyen, N. T., Kaul, U. K., Lebofsky, S., Ting, E., Chaparro, D., Urnes, J., "Development of Variable Camber Continuous Trailing Edge Flap for Performance Adaptive Aeroelastic Wing," SAE Paper 15ATC-0250, 2015

[13]Kaul, U. K. and Nguyen, N. T., "Drag Optimization Study of Variable Camber Continuous Trailing Edge Flap (VCCTEF) Using OVERFLOW," AIAA 2014-2444, 32nd Applied Aerodynamics Conference, Atlanta, GA, June 2014

[14]Nguyen, N. T., Precup, N., Livne, L., Urnes, J., Dickey, E., Nelson, C., Chiew, J., Rodriguez, D., Ting, E., and Lebofsky, S., "Wind Tunnel Investigation of a Flexible Wing High-Lift Configuration with a Variable Camber Continuous Trailing Edge Flap Design," 33rd AIAA Applied Aerodynamics Confererence, AIAA-2015-2417, June 2015.

[15]Nguyen, N., Precup, N., Urnes, J., Nelson, C., Lebofsky, S., Ting, E., and Livne, E., "Experimental Investigation of a Flexible Wing with a Variable Camber Continuous Trailing Edge Flap Design," 32nd AIAA Applied Aerodynamics, AIAA 2014-2441, June 2014.

[16]Nguyen, N., Ting, E., and Lebofsky, S., "Aeroelastic Analysis of Wind Tunnel Test Data of a Flexible Wing with a Variable Camber Continuous Trailing Edge Flap," 56th AIAA/ASME/ASCE/AHS/ASC Structures, Structural Dynamics, and Materials Conference, AIAA-2015-1405, January 2015.

[17] Nathan Precup, Marat Mor and Eli Livne, "The Design, Construction, and Tests of a Concept Aeroelastic Wind Tunnel Model of a High-Lift Variable Camber Continuous Trailing Edge Flap (HL-VCCTEF) Wing Configuration," AIAA 2015-1406, 56th AIAA/ASCE/AHS/ASC Structures, Structural Dynamics, and Materials Conference 5-9 January 2015, Kissimmee, Florida,

[18]Tikhonov, A. N., "Regularization of incorrectly posed problems," Sov. Math. Dokl, 4:1624Đ1627, 1963

7 Figures

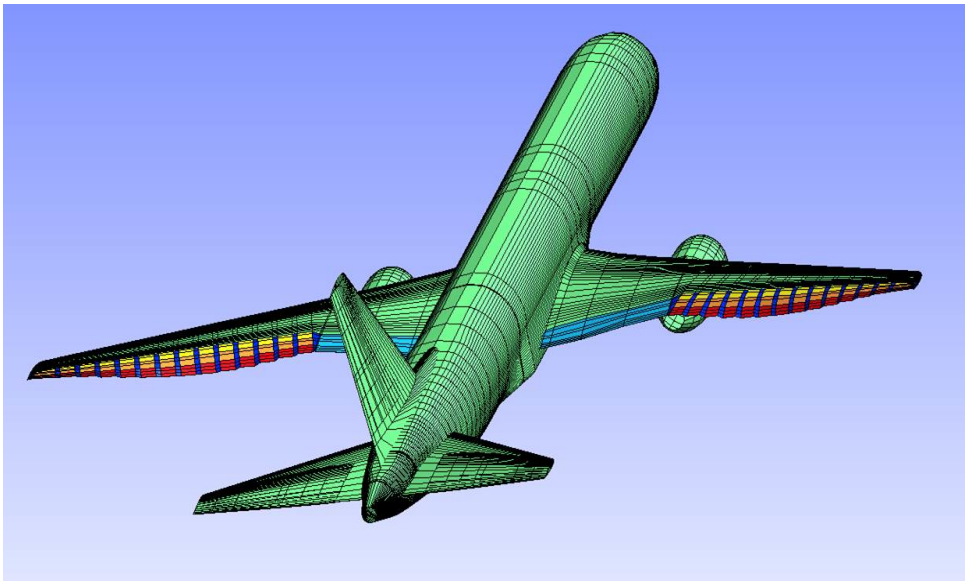

Figure 1: VCCTEF deployed on the generic transport model (GTM).

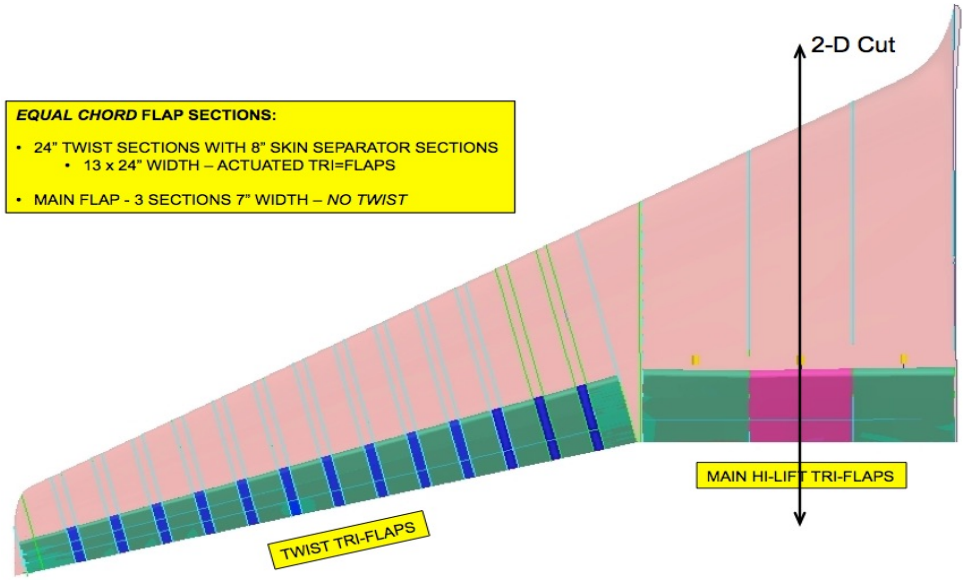

Figure 2: NASA/Boeing VCCTEF Configuration.

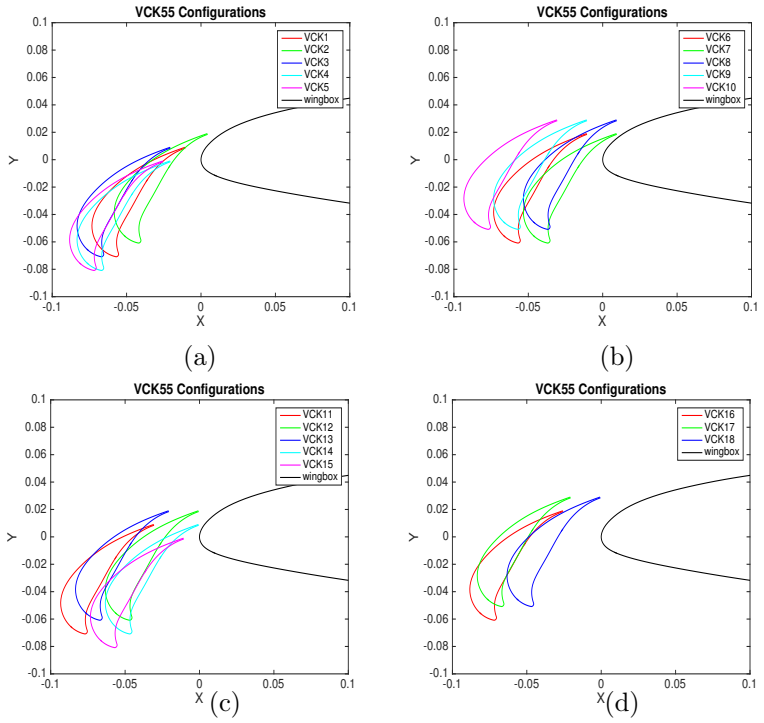

Figure 3: VCK55: Various *vck* configurations.

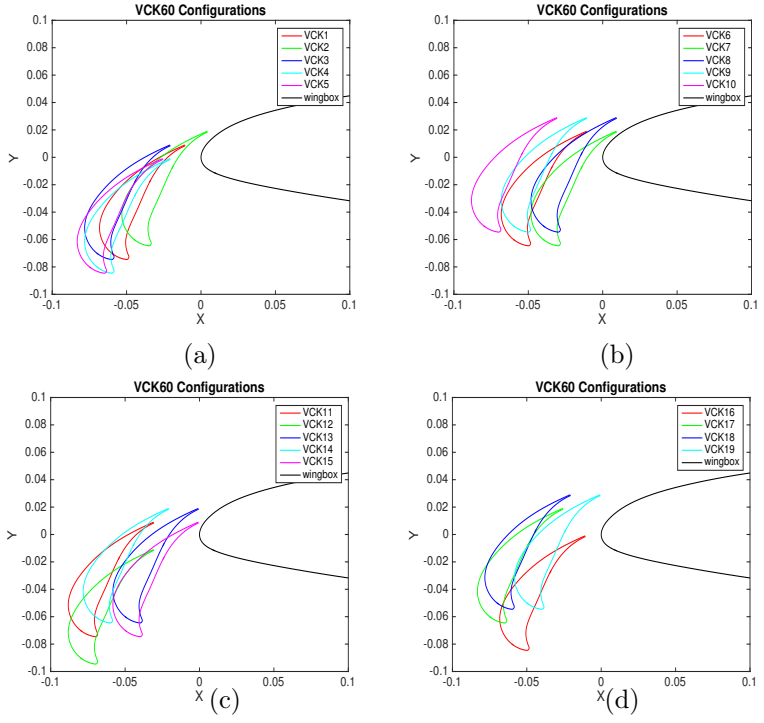

Figure 4: VCK60: Various *vck* configurations.

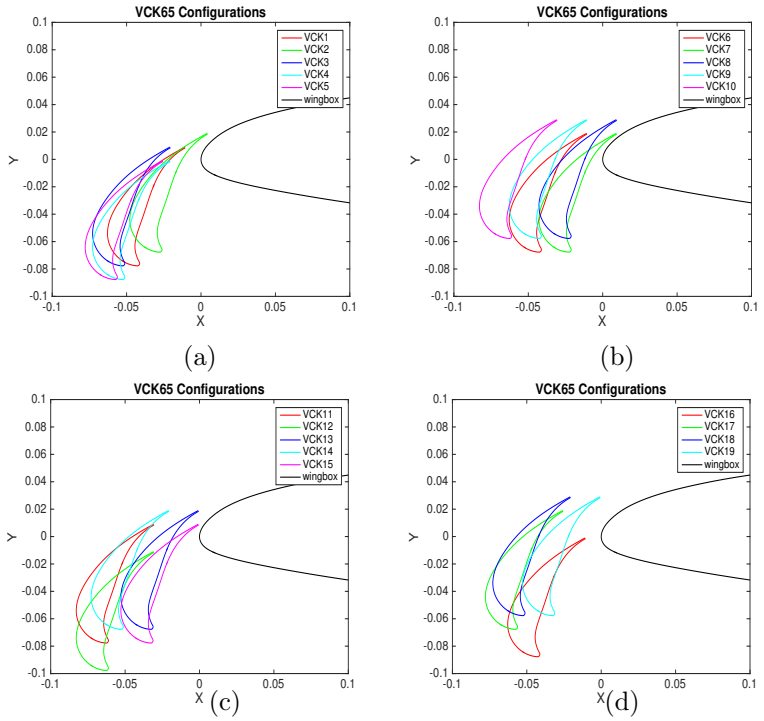

Figure 5: VCK65: Various *vck* configurations.

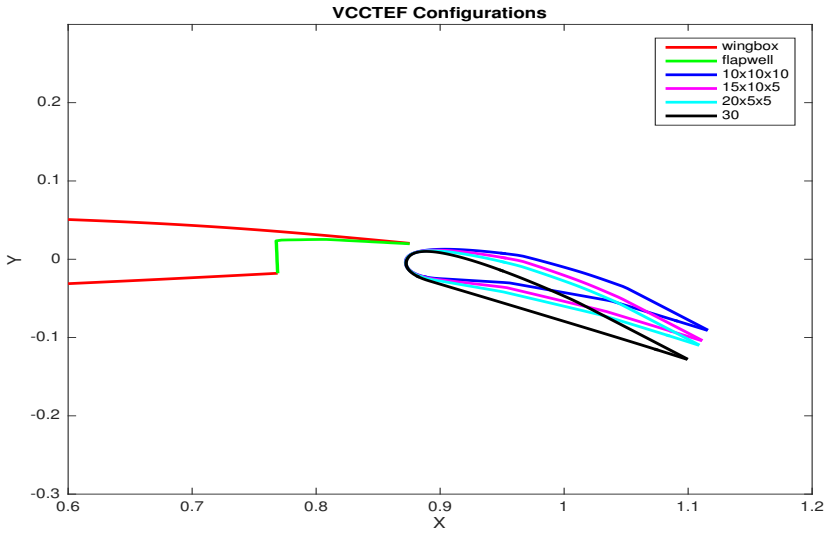

Figure 6: Four VCCTEF settings.

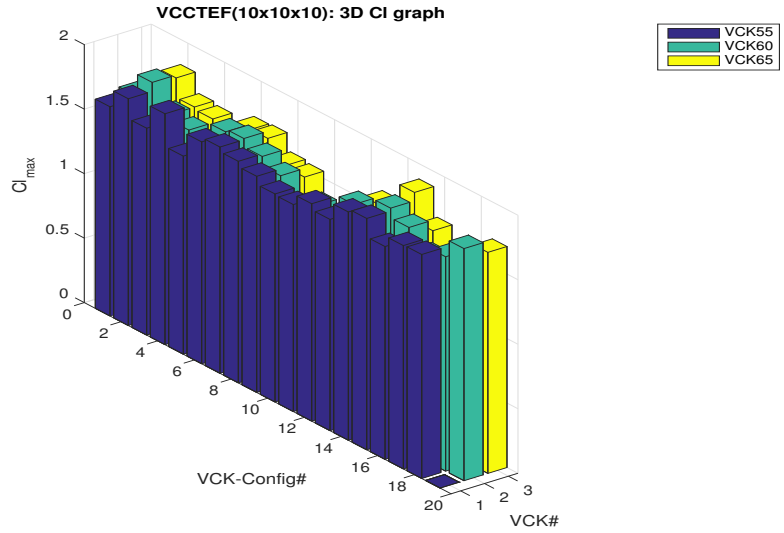

Figure 7: 3D bar graph showing C_{lmax} for VCCTEF 10x10x10 setting

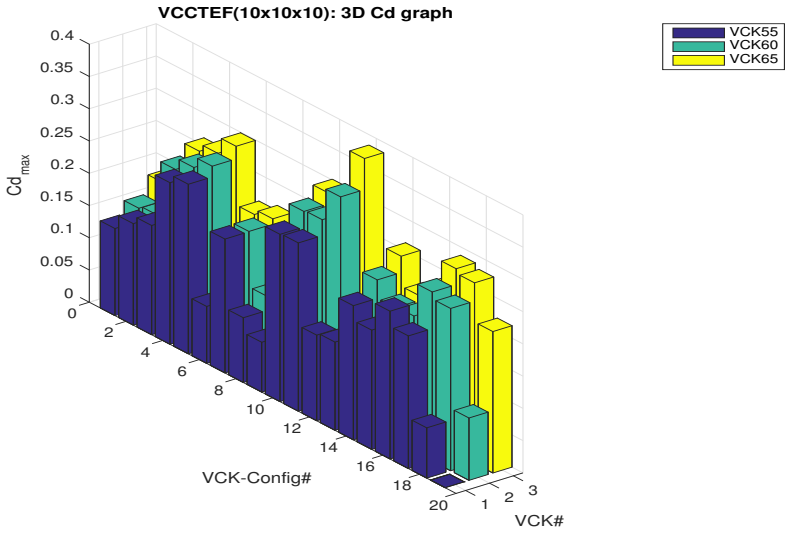

Figure 8: 3D bar graph showing C_{dmax} for VCCTEF 10x10x10 setting

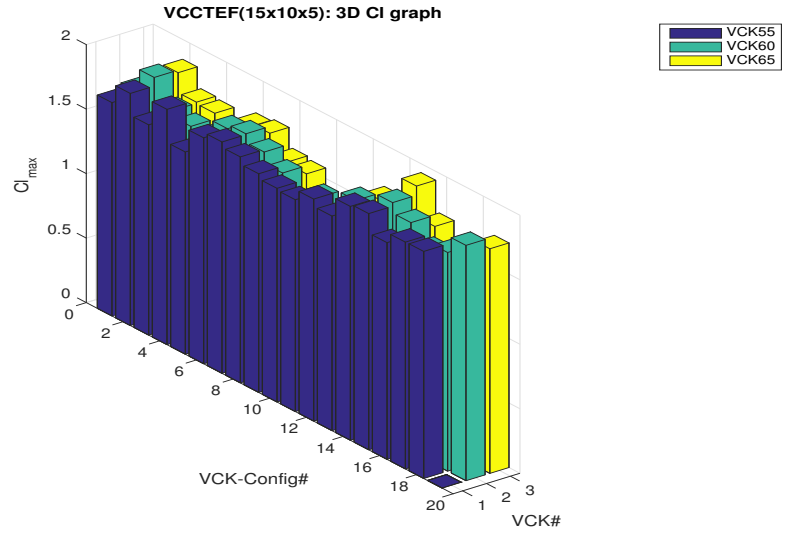

Figure 9: 3D bar graph showing C_{lmax} for VCCTEF 15x10x5 setting

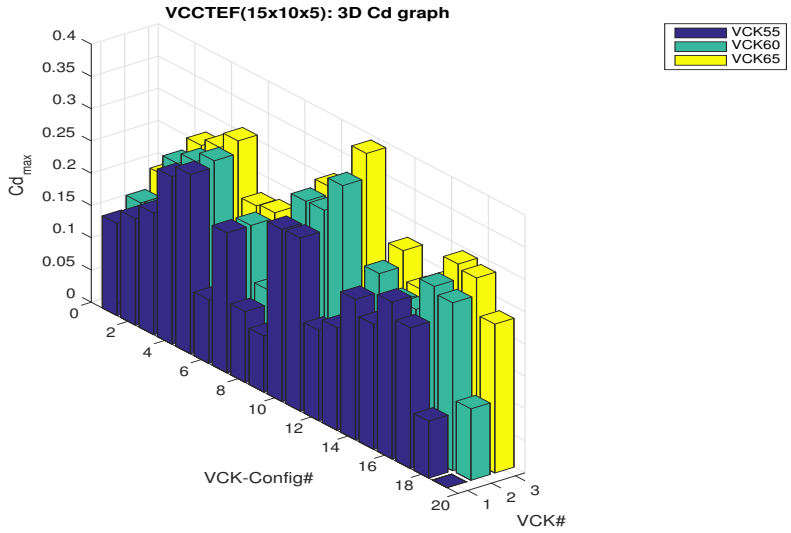

Figure 10: 3D bar graph showing C_{dmax} for VCCTEF 15x10x5 setting

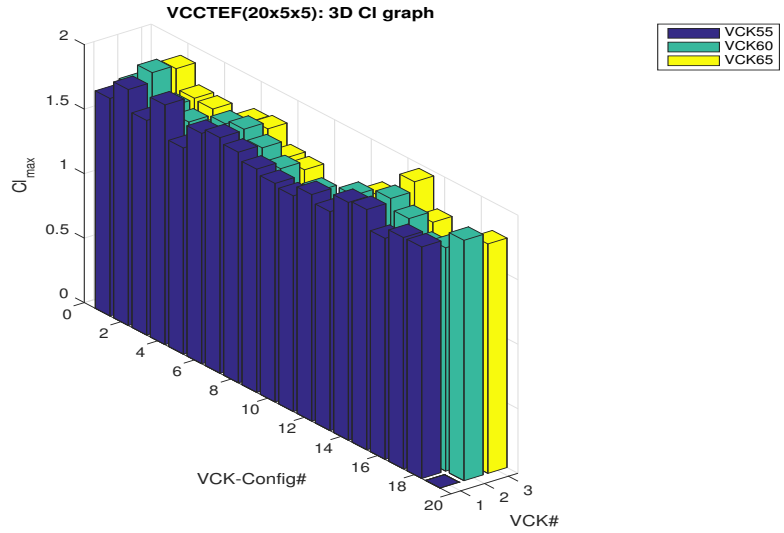

Figure 11: 3D bar graph showing C_{lmax} for VCCTEF 20x5x5 setting

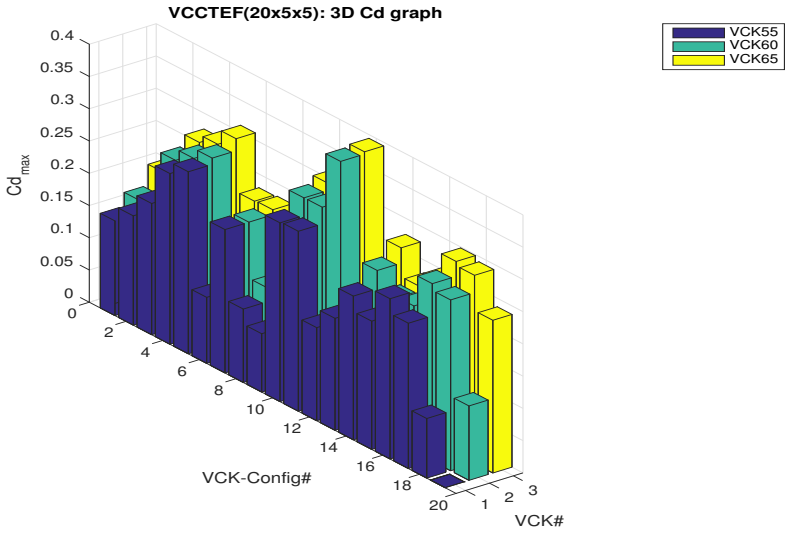

Figure 12: 3D bar graph showing C_{dmax} for VCCTEF 20x5x5 setting

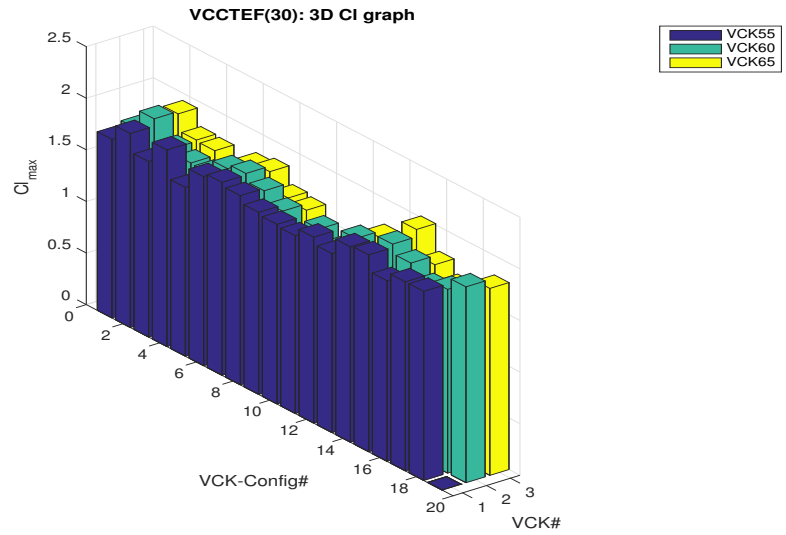

Figure 13: 3D bar graph showing C_{lmax} for VCCTEF 30x0x0 setting

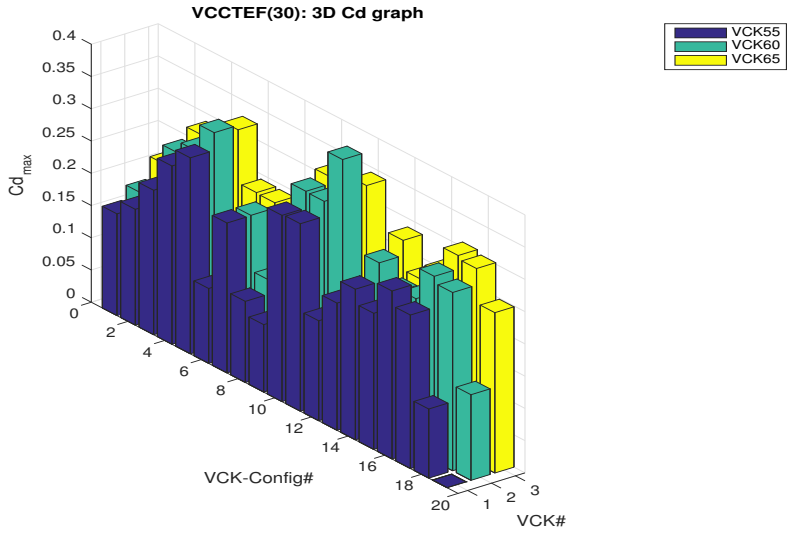

Figure 14: 3D bar graph showing C_{dmax} for VCCTEF 30x0x0 setting

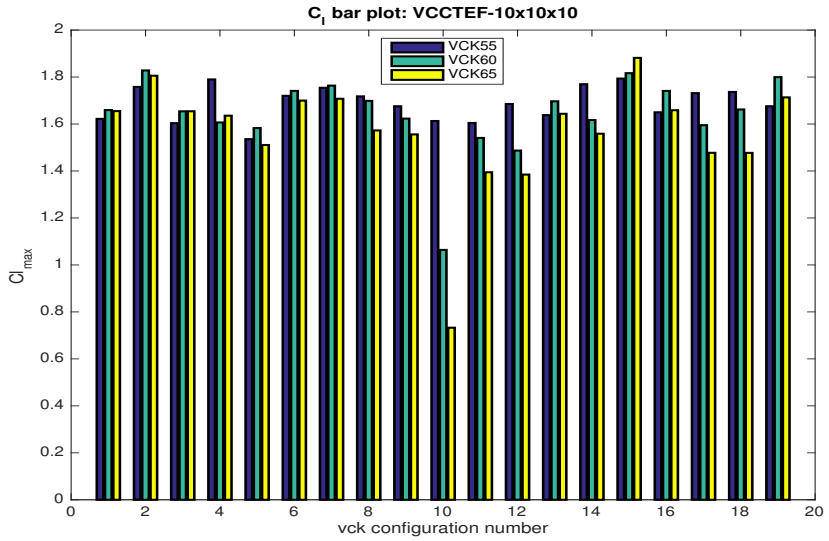

Figure 15: Bar graph showing C_{lmax} for VCCTEF-10x10x10 setting

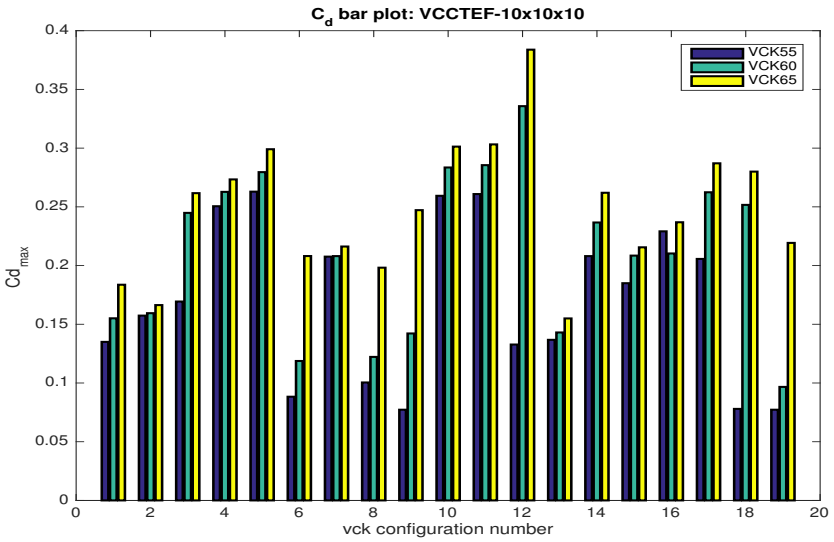

Figure 16: Bar graph showing C_{dmax} for VCCTEF-10x10x10 setting

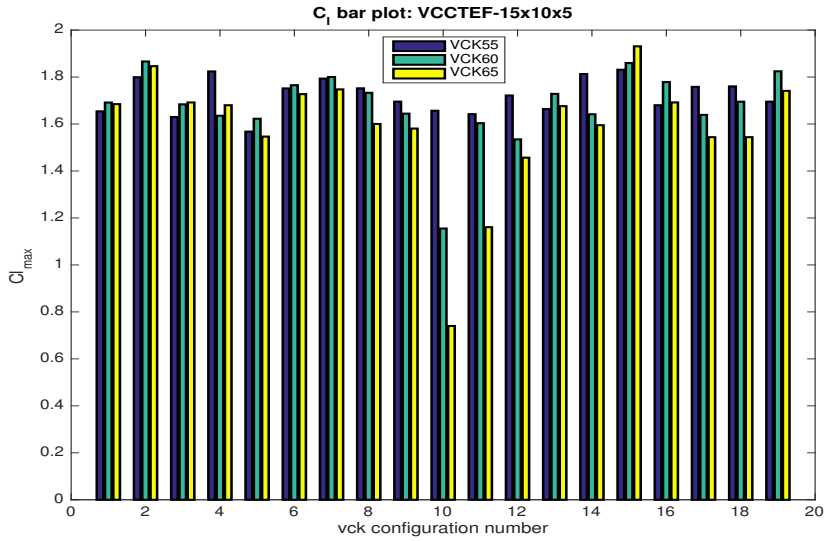

Figure 17: Bar graph showing C_{lmax} for VCCTEF-15x10x5 setting

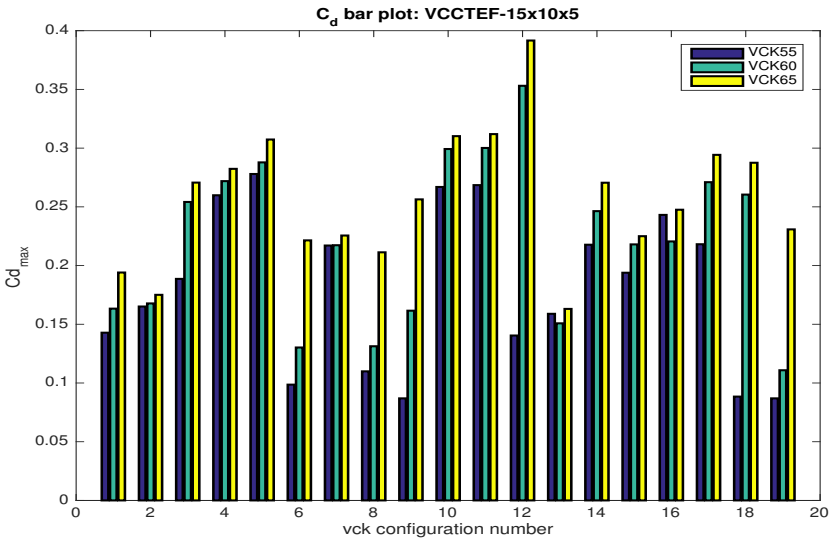

Figure 18: Bar graph showing C_{dmax} for VCCTEF-15x10x5 setting

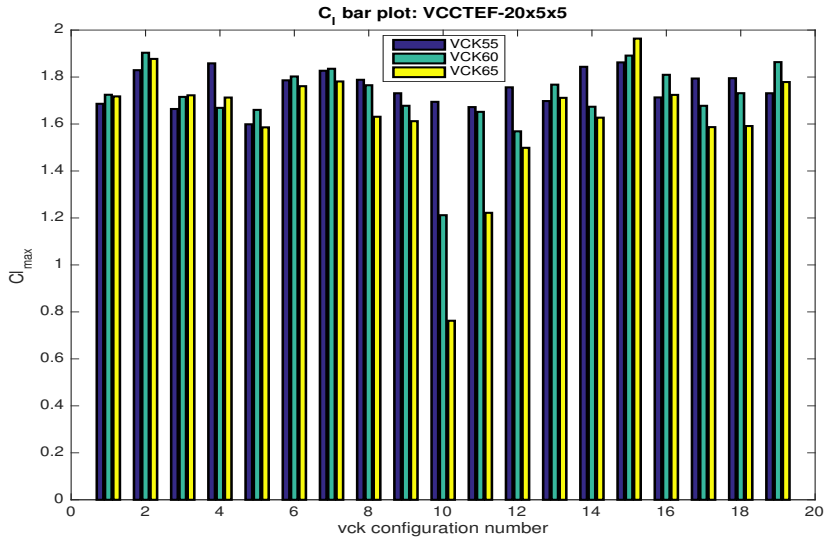

Figure 19: Bar graph showing C_{lmax} for VCCTEF-20x5x5 setting

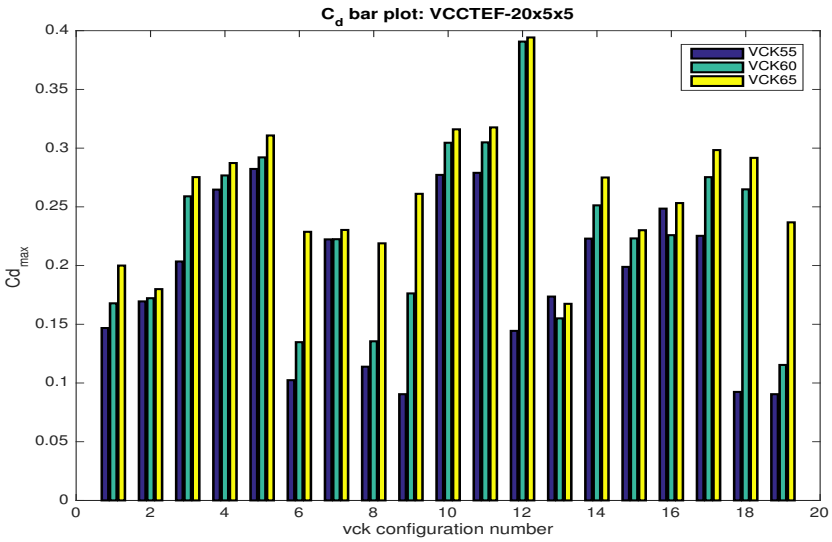

Figure 20: Bar graph showing C_{dmax} for VCCTEF-20x5x5 setting

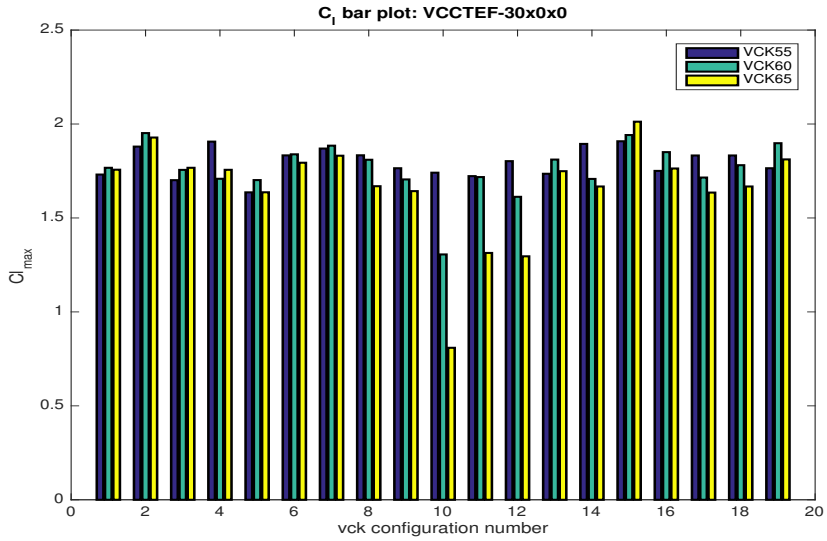

Figure 21: Bar graph showing C_{lmax} for VCCTEF-30x0x0 setting

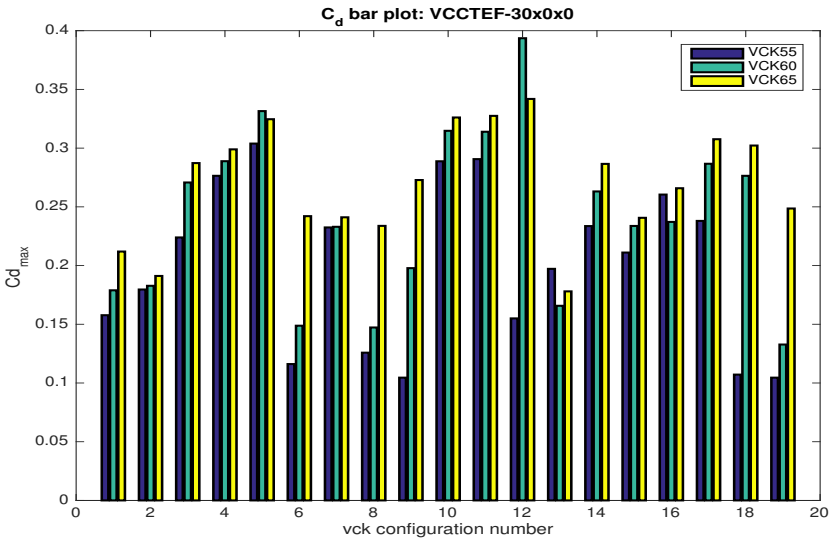

Figure 22: Bar graph showing C_{dmax} for VCCTEF-30x0x0 setting

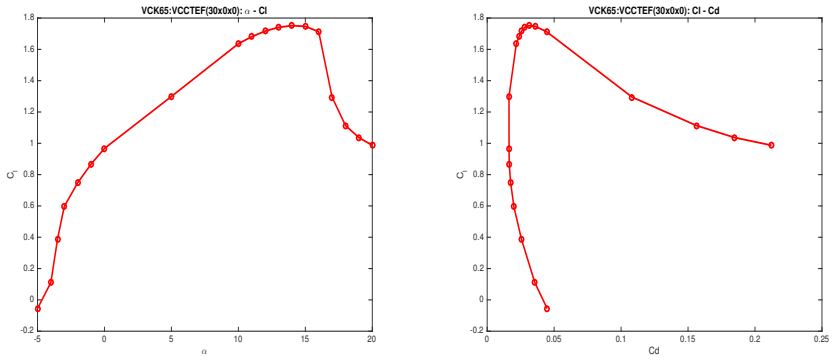

(a) C_l versus α (b) Drag polar

Figure 23: VCK65 results for the vck1 configuration and VCCTEF-30x0x0 setting

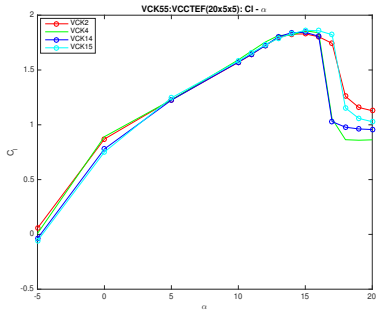

(a) C_l versus α

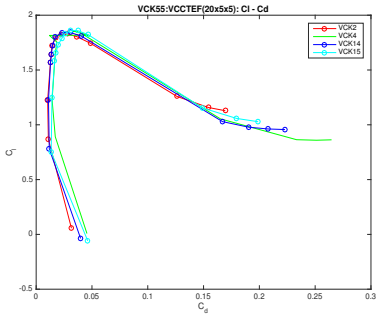

(b) Drag polar

Figure 24: VCK55 results for the VCCTEF-20x5x5 setting

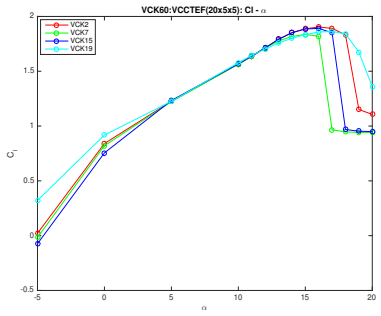

(a) C_l versus α

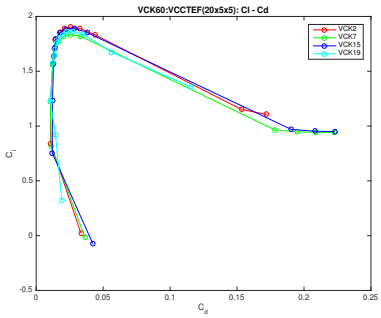

(b) Drag polar

Figure 25: VCK60 results for the VCCTEF-20x5x5 setting

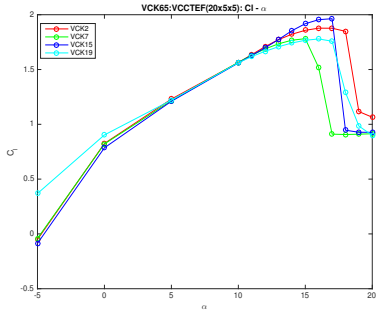

(a) C_l versus α

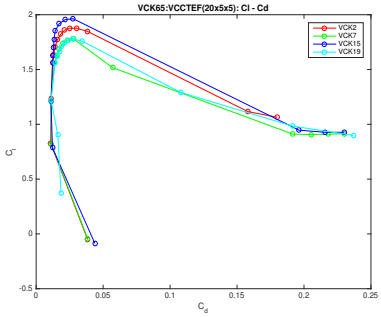

(b) Drag polar

Figure 26: VCK65 results for the VCCTEF-20x5x5 setting

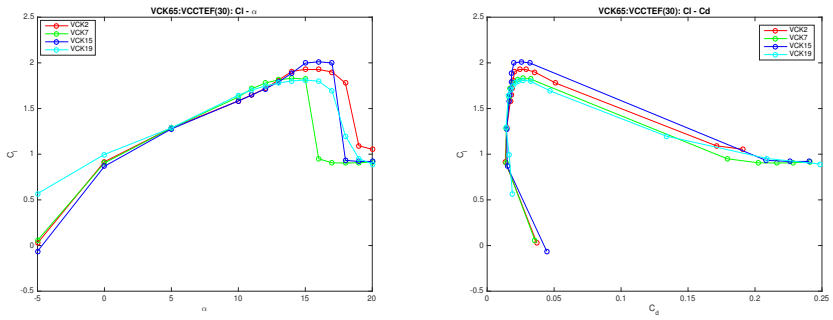

(a) C_l versus α (b) Drag polar

Figure 27: VCK65 results for the VCCTEF-30x0x0 setting

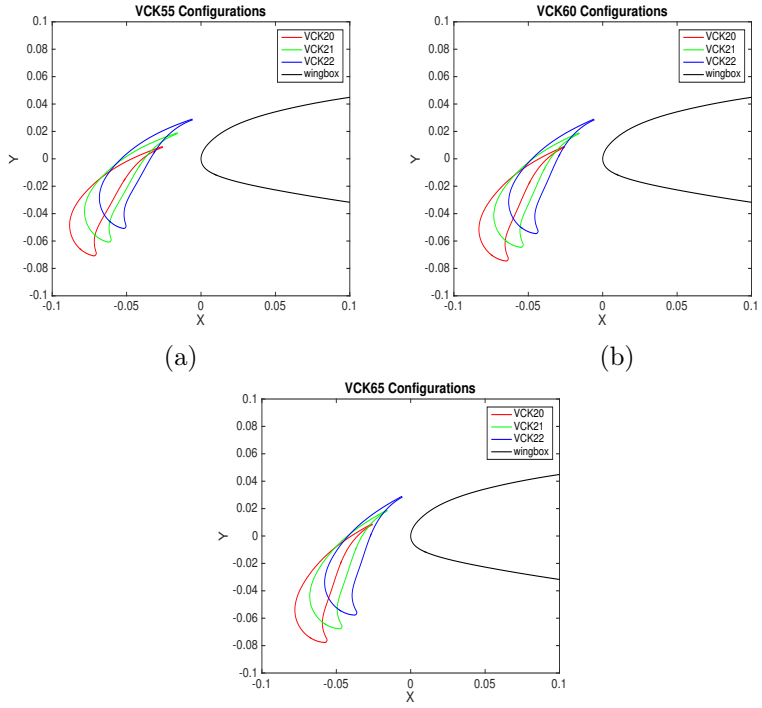

(a) (b)

(c)

Figure 28: VCK55/VCK60/VCK65: Test *vck* configurations for Learning Algorithm.

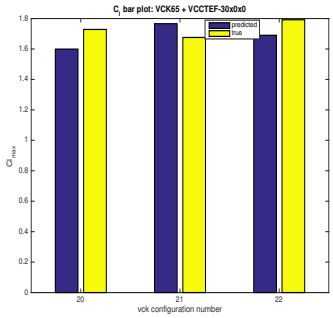

(a) VCK55 setting

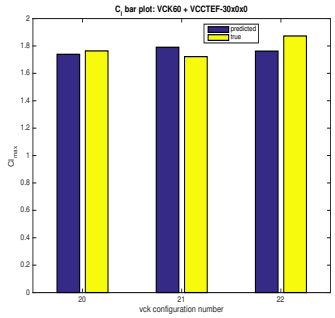

(b) VCK60 setting

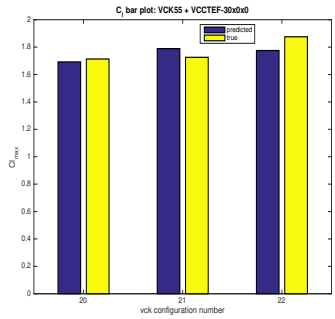

(c) VCK65 setting

Figure 29: Fully Supervised Algorithm: Predicted versus True C_{lmax}.

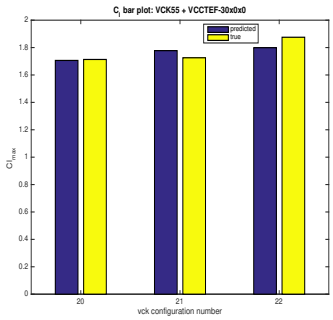

(a) VCK55 setting

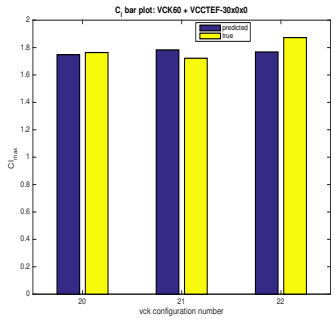

(b) VCK60 setting

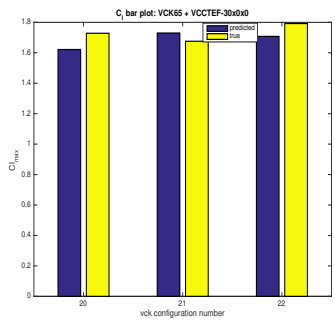

(c) VCK65 setting

Figure 30: Semi-supervised Algorithm: Predicted versus True C_{lmax}.

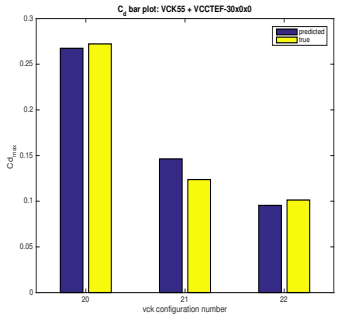

(a) VCK55 setting

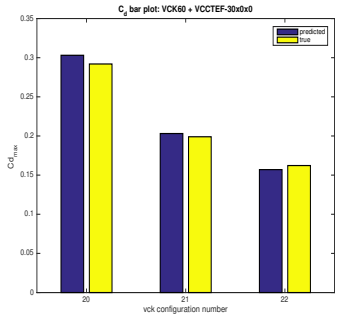

(b) VCK60 setting

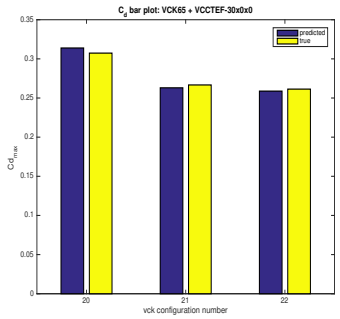

(c) VCK65 setting

Figure 31: Fully Supervised Algorithm: Predicted versus True C_{dmax}.

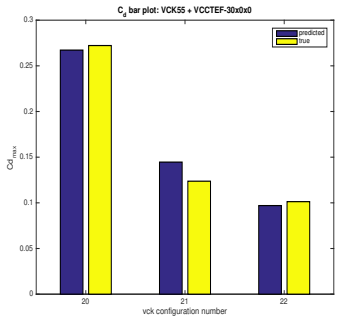

(a) VCK55 setting

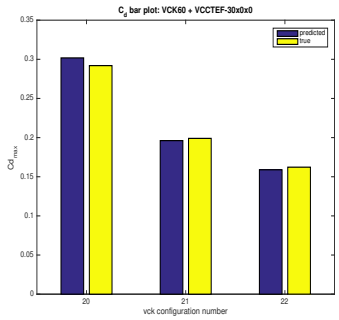

(b) VCK60 setting

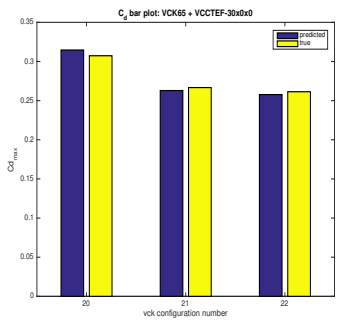

(c) VCK65 setting

Figure 32: Semi-supervised Algorithm: Predicted versus True C_{dmax}.